

# Deep Fourier-embedded Network for RGB and Thermal Salient Object Detection

Pengfei Lyu, Pak-Hei Yeung, Xiaosheng Yu, Chengdong Wu, and Jagath C. Rajapakse, *Fellow, IEEE*

**Abstract**—The rapid development of deep learning has significantly improved salient object detection (SOD) combining both RGB and thermal (RGB-T) images. However, existing deep learning-based RGB-T SOD models suffer from two major limitations. First, Transformer-based models with quadratic complexity are computationally expensive and memory-intensive, limiting their application in high-resolution bi-modal feature fusion. Second, even when these models converge to an optimal solution, there remains a frequency gap between the prediction and ground-truth. To overcome these limitations, we propose a purely Fourier transform-based model, namely Deep Fourier-Embedded Network (DFENet), for accurate RGB-T SOD. To address the computational complexity when dealing with high-resolution images, we leverage the efficiency of fast Fourier transform with linear complexity to design three key components: (1) the Modal-coordinated Perception Attention, which fuses RGB and thermal modalities with enhanced multi-dimensional representation; (2) the Frequency-decomposed Edge-aware Block, which clarifies object edges by deeply decomposing and enhancing frequency components of low-level features; and (3) the Fourier Residual Channel Attention Block, which prioritizes high-frequency information while aligning channel-wise global relationships. To mitigate the frequency gap, we propose Co-focus Frequency Loss, which dynamically weights hard frequencies during edge frequency reconstruction by cross-referencing bi-modal edge information in the Fourier domain. Extensive experiments on four RGB-T SOD benchmark datasets demonstrate that DFENet outperforms fifteen existing state-of-the-art RGB-T SOD models. Comprehensive ablation studies further validate the value and effectiveness of our newly proposed components. The code is available at <https://github.com/JoshuaLPF/DFENet>.

**Index Terms**—Fast Fourier transform, global dependency, RGB and thermal modalities, salient object detection.

## I. INTRODUCTION

**S**ALIENT object detection (SOD) identifies the most attention-grabbing objects in a scene, with broad applica-

This work was supported in part by the National Natural Science Foundation of China under Grant U20A20197 and 62306187, the Foundation of Ministry of Industry and Information Technology TC220H05X-04, Liaoning Key Research and Development Project under Grant 2020JH2/10100040, Natural Science Foundation of Liaoning Province under Grant 2021-KF-12-01, the Foundation of National Key Laboratory under Grant OEIP-O-202005, the Fundamental Research Fund for the Central Universities of China under Grant N2326001 and the China Scholarship Fund. (*Corresponding author: Chengdong Wu and Jagath C. Rajapakse*).

Pengfei Lyu is with the Faculty of Robot Science and Engineering, Northeastern University, Shenyang, 110169 China, and also with the College of Computing and Data Science, Nanyang Technological University, 639798 Singapore (e-mail:lyupengfei@stumail.neu.edu.cn).

Pak-Hei Yeung and Jagath C. Rajapakse are with the College of Computing and Data Science, Nanyang Technological University, 639798 Singapore (e-mail: pakhei.yeung@ntu.edu.sg; asjagath@ntu.edu.sg).

Xiaosheng Yu and Chengdong Wu are with the Faculty of Robot Science and Engineering, Northeastern University, Shenyang, 110169 China (e-mail: yuxiaosheng@mail.neu.edu.cn; wuchengdong@mail.neu.edu.cn).

tions spanning image compression [1], object recognition [2], scene perception [3], and more. Despite significant progress being made in RGB-based salient object detection [4]–[6], it remains challenging to separate salient objects from complex backgrounds or low-contrast scenes. To address this challenge, depth information was introduced to complement RGB features, enhancing the understanding of scenes [7]–[10].

However, the accuracy and stability of depth information are susceptible to environmental factors, such as varying light intensity, occlusions, and other conditions, limiting its applicability. In contrast, thermal infrared information offers distinct advantages in environmental adaptability. Even under adverse weather or low-light conditions, thermal images can effectively characterize objects by capturing their infrared radiations. As a result, RGB and thermal (RGB-T) SOD has gained increasing attention [11]–[14].

The Transformer architecture [15] has demonstrated excellent ability to acquire global dependencies, outperforming convolutional neural networks (CNNs) in various computer vision tasks [16], [17]. This success has led to the development of Transformer-based models for RGB-T SOD, which have achieved impressive performance [18]–[23]. However, a significant challenge arises from the high memory consumption and computational complexity of Transformers, particularly when handling high-resolution bi-modal features and inputs [23]. To mitigate these computational expenses during training, existing Transformer-based models usually employ compromise strategies, such as constructing CNN-based fusion modules [18]–[21], utilizing CNN-based backbones [21], [22], restricting Multi-head Self-attention (MHSA)-based modules to low-resolution feature fusion [7], [24], [25], and developing lightweight student models [26]. Despite these efforts, these approaches only partially explore global relationships, leading to less effective performance. This raises the question: is there a more efficient operation that can capture global relationships without compromising computational efficiency.

Recently, benefiting from its powerful global representation capabilities, fast Fourier transform (FFT) [27] has demonstrated remarkable performance in image enhancement tasks [28]–[31]. Notably, FFT is a global-based transform that represent all previous elements with each transformed element, making it memory-efficient. Inspired by this observation, we propose the purely FFT-based **DFENet** that aims to achieve high-resolution RGB-T SOD and bi-modal feature fusion by aligning global dependencies at every stage.

The differences in imaging techniques between RGB and thermal modalities result in vast disparities in information distribution. As a result, while both modalities depict the same

salient objects, they differ in the degree of saliency in the spatial dimension and exhibit distinct patterns in the channel dimension. To address this problem, we propose **Modal-coordinated Perception Attention (MPA)**, a Transformer-like module designed to align and fuse the two modalities effectively across both spatial and channel dimensions through a re-embedding strategy.

Given that SOD is a pixel-level dense prediction task, the decoding stage needs to integrate low-resolution encoder features from different levels to predict the high-resolution saliency map with detailed information. Therefore, it is important to prioritize high-frequency information in the decoding stage. However, the low-resolution high-level features tend to favor semantic information, while low-level features possess rich edge details but are accompanied by noisy textures. To overcome these challenges, we propose two novel components: the **Frequency-decomposed Edge-aware Block (FEB)** and the **Fourier Residual Channel Attention Block (FRCAB)**. Specifically, the FEB is designed to clarify edge features amidst cluttered textures by deeply decomposing low-level features, thereby guiding the integration of decoder features. Meanwhile, the FRCAB is applied at each decoder layer to mitigate excessive low-frequency pattern information, allowing the model to focus on learning high-frequency details. By considering global dependencies between channels in the frequency domain, FRCAB adaptively adjusts the channel features, enhancing the model's discriminative learning capability.

Furthermore, neural networks inherently tend to lose vital visual details as they deepen, while reconstructing high-frequency edge information is prone to spectral bias [32], causing models to prioritize learning easier frequencies over the hard ones. However, existing edge modules based on spatial domain learning tend to generate sparse spectra [19], [26], [33], treating all frequencies equally and making it difficult to accurately characterize edges. To address these issues, inspired by [34]–[36], we propose the **Co-focus Frequency Loss (CFL)** to guide FEB in the frequency domain while optimizing the entire model. In CFL, we measure the prediction and ground-truth using the Fourier frequency distance and introduce original edge frequency information of RGB and thermal modalities as a cross-reference to dynamically weight hard frequencies. This approach leads to refined edge features that further improve the quality of the saliency map in spatial domain learning.

By integrating these components, DFENet efficiently fuses RGB and thermal modalities by utilizing complementary relationships from the frequency perspective, ultimately producing saliency maps with high accuracy.

In summary, the main contributions of this paper are as follows:

- We propose DFENet, an FFT-based model designed to achieve high-resolution RGB-T SOD and bi-modal feature fusion while minimizing memory consumption. Through comprehensive ablation studies, we verify the effectiveness of the proposed components, including MPA, FEB, FRCAB, and CFL.
- We conduct extensive experiments on four benchmark datasets and show that our proposed DFENet achieves

superior performance and robustness compared to fifteen existing state-of-the-art models. Notably, DFENet is able to process bi-modal inputs with resolution up to  $512 \times 512$  on an NVIDIA Tesla P100 GPU with 16GB of memory.

- To the best of our knowledge, DFENet is the first FFT-based supervised model for SOD tasks. This work demonstrates the strong potential of FFT-based operations for dense prediction, highlighting their unique advantages while also exploring their limited compatibility with spatial domain operations.

## II. RELATED WORK

### A. RGB and Depth Salient Object Detection (RGB-D SOD)

To address the limitations of RGB-based salient object detection, depth information is introduced to better perceive the shape and spatial relationships of objects. Existing RGB-D SOD models can be broadly categorized into two types: CNN-based and Transformer-based.

CNN-based RGB-D SOD models typically leverage foundational attention mechanisms, such as convolutional block attention module [37] utilized in [38]–[43], dilated convolution [44] employed in [45], [46] and atrous spatial pyramid pooling [47] utilized in [48]–[50]. In addition, Ji et al. [9] proposed an unsupervised network that automatically generates pseudo-labels through iterative refinement. In [8], a depth calibration and fusion framework was proposed to mitigate the effect of noise and ambiguity in depth images. Furthermore, Yao et al. [51] augmented semantic representation by integrating depth maps into the single-stream encoder.

To address the limitations imposed by the local connectivity of CNNs, several Transformer-based models [15], [17] have been proposed. Liu et al. [52] introduced three Vision Transformers [16] with shared weights to refine high-level fused features. The pure Transformer networks were proposed in [7], [25] for simultaneous salient object and edge detection. Sun et al. [24] employed the Swin Transformer [17] as a dual-stream encoder, utilizing Multi-head Self-attention (MHSA) to handle high-level features. Wu et al. [10] proposed a cross-modality interaction parallel Transformer to fuse RGB and depth features, complemented by a contrast learning strategy. In contrast to these Transformer-based spatial domain models, our proposed DFENet employed Fourier Transform (FFT)-based operations to solve bi-modal SOD in the frequency domain.

### B. RGB and Thermal Salient Object Detection (RGB-T SOD)

In complex environments with varying lighting conditions or occlusions, depth information can become unreliable. To address this limitation, researchers [11]–[13] have introduced thermal modality as an alternative to depth information for SOD. Thermal imaging captures the infrared radiation emitted by objects and is more adaptable to different environmental conditions.

Similar to RGB-D SOD (Sec. II-A), recent efforts in RGB-T SOD primarily focus on inter-modal fusion. Several CNN-based fusion strategies have been proposed [14], [53]–[59] to combine multi-modal, multi-scale, and multi-granular features.

For example, Song et al. [14] utilized graph structures to reduce the impact of negative information. Inspired by style transfer, Chen et al. [57] devised a modal transfer mechanism to bridge complementary features. In addition, Tu et al. [60] proposed a weak alignment model for RGB and thermal modalities. Cong et al. [61] re-examined the role of thermal modality in relation to light variations.

To capture long-range relationships, researchers have introduced Transformers for various purposes, including use as backbones [18]–[20], post-processing of fused features [20], [21], or feature fusion [22]. In [22], Pang et al. proposed a cross-modal and cross-scale Transformer with a token re-embedding strategy to alleviate complexity. However, the substantial memory consumption of MHSA makes it challenging to apply Transformers in each stage of the model. A pure transformer model [23] using the Swin Transformer [17] in both encoder and decoder required four RTX3090 GPUs for training due to its computational demands.

To address the expensive computation, several studies [33], [62], [63] have explored lightweight modeling, but their performance has often fallen short of expectations. Zhou et al. [26] employed knowledge distillation, designing a wavelet transform-based WaveNet to acquire semantic and geometric knowledge from a complex teacher model [19]. Despite its merits, the wavelet transform is inherently locally based and fails to capture long-range dependencies effectively.

Considering these limitations, we design a purely FFT-based DFENet. The FFT is a globally based transform that has an advantage over MHSA and the wavelet transform in efficiently obtaining global relationships. This property allows each component of DFENet to access and optimize global relationships effectively. Moreover, DFENet offers memory efficiency and supports input resolution up to  $512^2$  on an NVIDIA Tesla P100 GPU with 16GB of memory (see Sec. IV-C for details).

### C. Fast Fourier Transform (FFT)-based Networks

Despite the recent advancement achieved by MHSA-based Transformers [16], [17] in various tasks, the trade-off between the perceived field size and computational cost remains a challenge. To address this problem, researchers have explored alternative approaches based on the FFT. For example, Rao et al. [64] proposed an FFT-based global filter to learn long-distance dependencies with linear complexity. Guibas et al. [65] constructed a token mixer as a globally continuous convolution, while Tatsunami et al. [66] incorporated the concept of data correlation into the global filter to dynamically extract image features. Despite these advancements, existing works have primarily focused on the spatial dimension, overlooking the exploration of intrinsic discriminative features in the channel dimension. Zhou et al. [67] addressed this limitation by designing two branches to perform FFT in both spatial and channel dimensions for image restoration.

Meanwhile, researchers have also applied FFT-based models for various downstream tasks, including image enhancement [28]–[31], image inpainting [68], image compression [36], and image reconstruction [69], [70]. However, there is a notable

scarcity of research on dense prediction tasks. Existing dense prediction models [71], [72] typically focus on high- and low-frequency components of the Fourier signal, neglecting deeper components such as amplitude and phase.

In this paper, we proposed DFENet to develop FFT for addressing dense prediction tasks, specifically SOD. To the best of our knowledge, this is the first FFT-based supervised model specifically designed for this task.

## III. METHODS

### A. Overview

In this section, we introduce the proposed DFENet, a novel architecture designed for RGB and thermal salient object detection (RGB-T SOD), as illustrated in Fig. 1.

The network begins with a dual-stream encoder based on fast Fourier transform (FFT)-based CDFFormer-m [66], which processes the RGB and thermal modalities separately to extract set of features at four different scales, denoted as  $\{r_i\}_{i=1}^4$  and  $\{t_i\}_{i=1}^4$ , respectively.

The extracted features are then processed by our Modal-coordinated Perception Attention (MPA) (Sec. III-B), which is designed to obtain cross-modal fusion features  $\{f_i\}_{i=1}^4$ .

Subsequently,  $\{t_i, f_i\}_{i=1}^2$  are input into our Frequency-decomposed Edge-aware Block (FEB) (Sec. III-C), which is designed to extract detailed edge features  $\{e_i\}_{i=1}^3$ .

In the decoding stage, we employ a pyramid design to handle object scale variations. Each layer of the decoder concatenates the corresponding fusion feature  $f_i$  with features from all previous layers. These concatenated features are then refined using our Fourier Residual Channel Attention Block (FRCAB) (Sec. III-D), resulting in refined features  $\{d_i\}_{i=1}^4$ .

Finally, the network is optimized using a bi-domain learning approach (Sec. III-E), which combines the proposed Co-focus Frequency Loss (CFL)  $\mathcal{L}_{CFL}$ , binary cross-entropy loss (BCE) [73]  $\mathcal{L}_{BCE}$ , and intersection-over union loss (IoU) [74]  $\mathcal{L}_{IoU}$ .  $\mathcal{L}_{CFL}$  in the frequency domain facilitates global optimization, prioritizing the resolution of hard frequencies during the edge-frequency reconstruction process. Meanwhile,  $\mathcal{L}_{BCE}$  and  $\mathcal{L}_{IoU}$  in the spatial domain achieve substantial pixel-wise saliency prediction  $\mathcal{S}$ .

### B. Modal-coordinated Perception Attention (MPA)

The differences in feature distribution between RGB and thermal modalities stem from their distinct physical meanings, encapsulating complementary information. Specifically, while objects share the same spatial location across both modalities, they exhibit varying degrees of saliency, leading to differences in spatial representation. The RGB modality provides richer appearance and texture details, whereas the thermal modality emphasizes overall shape and structure. As a result, the importance of feature channels differs across modalities [19]. This observation highlights the need to align and integrate bi-modal features in both spatial and channel dimensions.

To address these challenges, we propose the MPA to effectively integrate and align information from both modalities. MPA employs a re-embedding strategy, which first extracts the spatial Fourier components from both modalities and

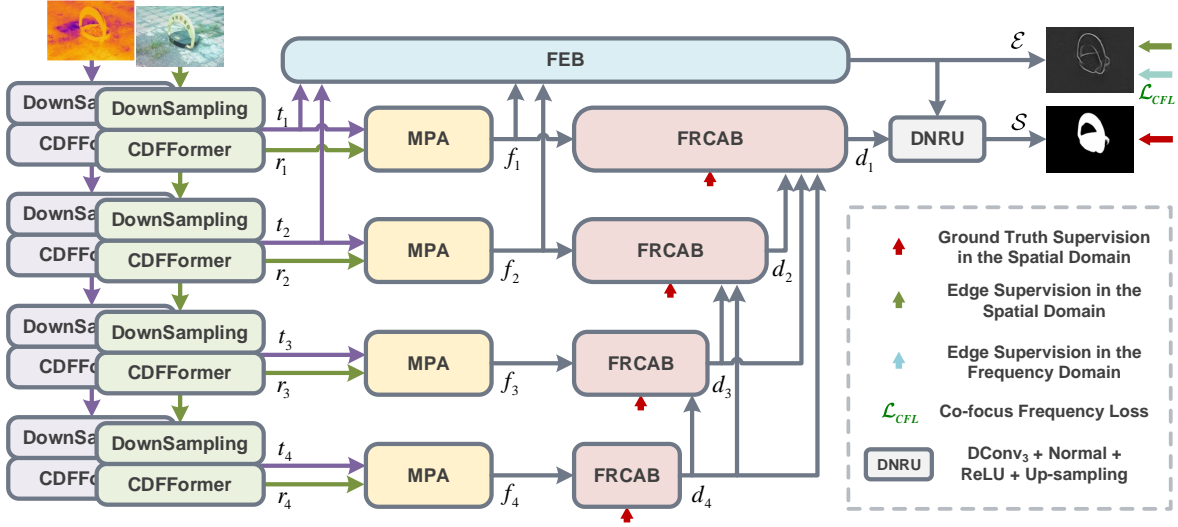


Fig. 1. The framework of our proposed DFENet. RGB and thermal images are first extracted initial features  $\{r_i\}_{i=1}^4$  and  $\{t_i\}_{i=1}^4$  by a dual-stream encoder. Next, the bi-modal features enter the Modal-coordinated Perception Attention (MPA) to bridge the complementary information and fuse. During decoding, the fused features  $\{f_i\}_{i=1}^4$  are integrated in a low- to high-resolution manner by Fourier Residual Channel Attention Block (FRCAB) to obtain decoder features  $\{d_i\}_{i=1}^4$ . Meanwhile, the shallow features  $\{t_i, f_i\}_{i=1}^2$  are fed into the Frequency-decomposed Edge-aware Block (FEB) to obtain elaborate edge features  $\{e_i\}_{i=1}^3$  for guiding the decoding process in generating the accurate saliency map  $S$ . In the training stage, the Co-focus Frequency Loss (CFL)  $\mathcal{L}_{CFL}$  favoring the synthesis of difficult frequencies and spatial-domain losses are employed together to supervise the generation of the high-quality edge map  $\mathcal{E}$ .

then enhances the channel Fourier components for each spatial Fourier component separately. Notably, the spatial-based Fourier component serves as an efficient representation of global information, while delving into its channel-dimensional representation further enhances its descriptive power.

The diagram of MPA is shown in Fig. 2, which follows a Transformer-like structure of Transformer. It primarily consists of a Modal-coordinated Perception Filter (MPF), normalization layers  $Norm(\cdot)$ , a  $3 \times 3$  depth-wise separable convolution layer  $DConv_3(\cdot)$  in the feed-forward network, and residual connections. This process can be formulated as:

$$\tilde{f}_i = MPF(Norm(r_i), Norm(t_i)), i = 1, 2, 3, 4, \quad (1)$$

$$f_i = DConv_3(Norm(\tilde{f}_i + r_i + t_i)) + \tilde{f}_i + r_i + t_i, \quad (2)$$

where  $+$  is element-wise addition.  $\tilde{f}_i$  and  $f_i \in \mathbb{R}^{C \times H \times W}$  represent the output of MPF and MPA, respectively, with  $C$ ,  $H$ , and  $W$  denoting the number of channels, height, and width, respectively.

In MPF, we apply a sequence of operations to the normalized bi-modal features  $\tilde{r}_i$  and  $\tilde{t}_i$ : a  $1 \times 1$  convolution layer  $Conv_1(\cdot)$ , followed by a StarReLU [75] layer  $SR(\cdot)$ , and finally, a fast Fourier transform (FFT) in the spatial dimension, to obtain the spatial Fourier components  $f_i^{rs}$  and  $f_i^{ts}$ :

$$f_i^{rs} = FFT(SR(Conv_1(\tilde{r}_i))), \quad (3)$$

$$f_i^{ts} = FFT(SR(Conv_1(\tilde{t}_i))). \quad (4)$$

In the channel Fourier component enhancement stage, we extract the amplitude  $a_i^{rs}$  of  $f_i^{rs} \in \mathbb{R}^{C \times H \times (\frac{W}{2} + 1)}$  and  $a_i^{ts}$  of  $f_i^{ts} \in \mathbb{R}^{C \times H \times (\frac{W}{2} + 1)}$  for the secondary FFT in the channel dimension (CFFT), obtaining the channel Fourier components  $f_i^{rc}$  and  $f_i^{tc}$ :

$$a_i^{rs} = Amp(f_i^{rs}), a_i^{ts} = Amp(f_i^{ts}) \quad (5)$$

$$f_i^{rc} = CFFT(a_i^{rs}), f_i^{tc} = CFFT(a_i^{ts}). \quad (6)$$

We then enhance the amplitude and phase components using  $CLC_1(\cdot)$ , which consists of two  $Conv_1(\cdot)$  and a LeakyReLU layer. This process is applied to the amplitude component  $a_i^{rc}$ , the phase component  $p_i^{rc}$  of  $f_i^{rc} \in \mathbb{R}^{(\frac{C}{2} + 1) \times H \times (\frac{W}{2} + 1)}$  and  $a_i^{tc}$ ,  $p_i^{tc}$  of  $f_i^{tc} \in \mathbb{R}^{(\frac{C}{2} + 1) \times H \times (\frac{W}{2} + 1)}$ , respectively. After that, the channel-enhanced components are composed into complexes and undergo an inverse CFFT (ICFFT). The process is denoted as:

$$a_i^{rc} = Amp(f_i^{rc}), p_i^{rc} = Pha(f_i^{rc}), \quad (7)$$

$$\tilde{a}_i^{rs} = ICFFT(Complex(CLC_1(a_i^{rc}), CLC_1(p_i^{rc}))), \quad (8)$$

$$a_i^{tc} = Amp(f_i^{tc}), p_i^{tc} = Pha(f_i^{tc}), \quad (9)$$

$$\tilde{a}_i^{ts} = ICFFT(Complex(CLC_1(a_i^{tc}), CLC_1(p_i^{tc}))). \quad (10)$$

To effectively integrate the channel-enhanced components with the original amplitude components, we utilize a shortcut connection in each branch. Subsequently, we combine the amplitude and phase components of the spatial Fourier representations from both branches as complexes. We then employ an element-wise addition to facilitate complementarity of two modalities:

$$\tilde{f}_i^{rs} = Complex((a_i^{rs} \cdot \tilde{a}_i^{rs}), CLC_1(p_i^{rs})), \quad (11)$$

$$\tilde{f}_i^{ts} = Complex((a_i^{ts} \cdot \tilde{a}_i^{ts}), CLC_1(p_i^{ts})), \quad (12)$$

$$\tilde{f}_i^s = \tilde{f}_i^{rs} + \tilde{f}_i^{ts}, \quad (13)$$

In the spatial Fourier component enhancement stage, we introduce a dynamic filter  $DF(\cdot) \in \mathbb{R}^{C \times H \times (\frac{W}{2} + 1)}$  [66]

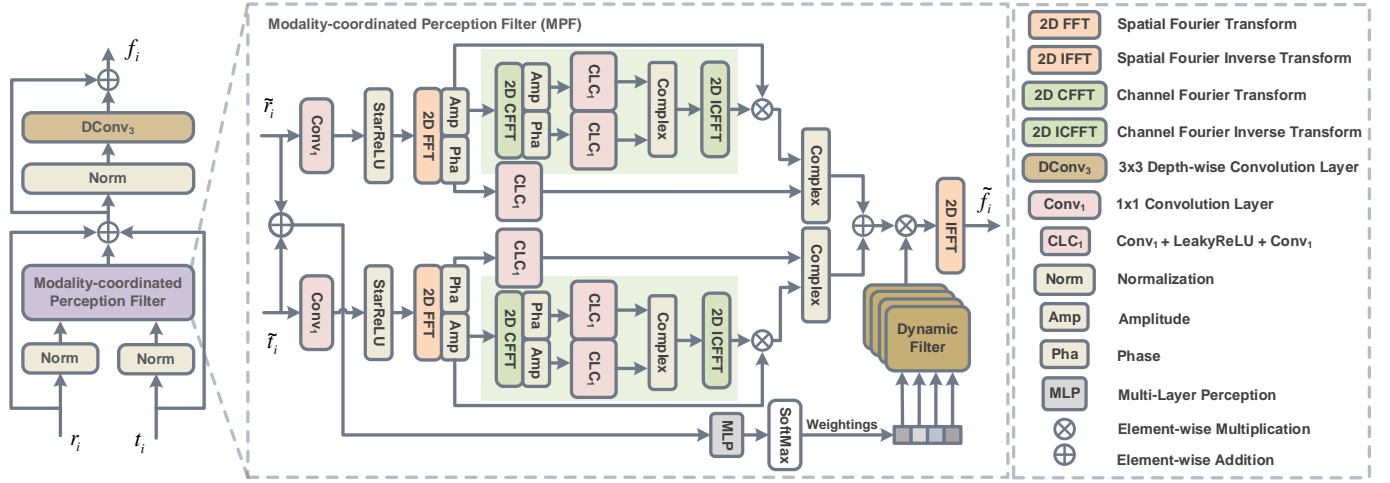


Fig. 2. Architectures of the Modal-coordinated Perception Attention (MPA) and its core component Modal-coordinated Perception Filter (MPF).

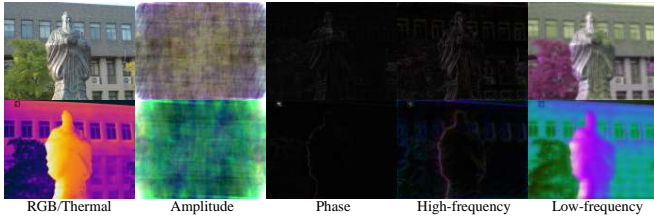


Fig. 3. The visualization for the amplitude, phase, high-frequency, and low-frequency components of RGB and thermal images.

to perform spatial filtering for the channel-enhanced fusion feature  $\tilde{f}_i^s$ .  $DF$  consists of  $N$  learnable filters  $\{LF_1, \dots, LF_N\}$  and a multi-layer perception  $MLP(\cdot)$  is used to assign weights for learnable filters. Additionally, we utilize  $\tilde{r}_i$  and  $\tilde{t}_i$  to provide initial weights for filters. This process can be formulated as:

$$\tilde{f}_i = IFFT \left( DF \left( \tilde{r}_i, \tilde{t}_i \right) \cdot \tilde{f}_i^s \right), \quad (14)$$

and

$$DF \left( \tilde{r}_i, \tilde{t}_i \right)_{j,:} = \sum_{n=1}^N \left( \frac{e^{S^{(j-1)N+n}}}{\sum_{m=1}^N e^{S^{(j-1)N+m}}} \right) LF_n, \quad (15)$$

where

$$\left( s_1, \dots, s_{NC} \right)^T = MLP \left( \frac{\sum_{h,w} \left( \tilde{r}_i + \tilde{t}_i \right)_{:,h,w}}{HW} \right), \quad (16)$$

where  $j$  represents the channel index,  $m$  and  $n$  denote filter indexes. In this paper,  $N$  is set to 8 to avoid over-computing in all experiments.

### C. Frequency-decomposed Edge-aware Block (FEB)

The precise identification of object details is crucial for improving detection performance. However, low-level features extracted from the initial layers of a network often contain boundary details alongside cluttered background noise and interference. This phenomenon poses a significant challenge for the decoder in making accurate predictions. To clarify

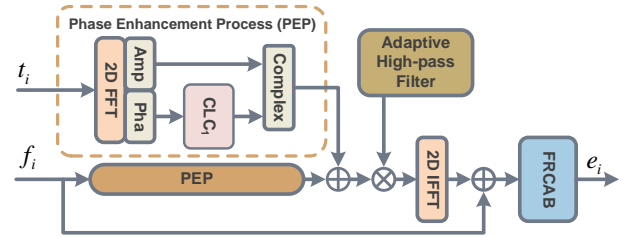


Fig. 4. Architecture of the Edge Frequency Extraction Block (EFEB).

boundary details and mitigate the impact of noise, we propose the FEB, a novel module specifically designed to provide the decoder with reliable edge features.

In Fig. 3, we present a decomposition of RGB and thermal images in the frequency domain. It can be observed that the amplitude and low-frequency components predominantly capture style and content information, whereas the phase and high-frequency components encapsulate detailed edges and textures. Furthermore, compared to RGB images, thermal images exhibit clearer object contours and less complex textures. Building on this observation, we develop a key component of the FEB, namely the Edge Frequency Extraction Block (EFEB), as illustrated in Fig. 4.

The FEB contains two EFEBs, which begin with  $\{t_i, f_i\}_{i=1}^2$  undergoing a Phase Enhancement Process (PEP) to highlight object boundaries, followed by integration. An adaptive high-pass filter  $HF$  is then employed to retain detailed edge information while removing style information. Finally, the output is refined by a Fourier Residual Channel Attention Block (FRCAB) to mitigate the neural network's preference for low-frequency information, with details provided in Sec. III-D.

In PEP, a given input  $x$  undergoes a FFT in the spatial dimension initially, followed by phase component enhancement. The PEP can be mathematically expressed as:

$$a^{xs} = Amp(FFT(x)), p^{xs} = Pha(FFT(x)), \quad (17)$$

$$\tilde{x} = Complex(a^{xs}, CLC_1(p^{xs})). \quad (18)$$

Then, EFEB can then be formulated as:

$$\tilde{e}_i = (PEP(t_i) + PEP(f_i)) \times HF, \quad (19)$$

$$e_i = FRCAB(IFFT(\tilde{e}_i) + f_i), i = 1, 2, \quad (20)$$

where  $\times$  is element-wise multiplication. Finally, the output edge feature  $e_3$  of FEB is calculated as:

$$e_3 = DNRU(Concat(e_1, UP_2(e_2))), \quad (21)$$

where  $UP_2(\cdot)$  represents  $2\times$  up-sampling, and  $Concat(\cdot)$  denotes concatenation.  $DNRU(\cdot)$  represents a set of operations including  $DCConv_3(\cdot)$ ,  $Norm(\cdot)$ , a ReLU layer, and  $UP_2(\cdot)$ .

#### D. Fourier Residual Channel Attention Block (FRCAB)

Due to the inherent bias of neural networks, low-resolution encoder features tend to emphasize low-frequency semantic information. However, for dense prediction tasks, the decoding stage should focus more on high-frequency components to generate precise high-resolution saliency maps. Additionally, as the channel dimensions are progressively reduced, treating all feature channels equally can hinder the generation of accurate saliency maps. To address these issues, we draw inspiration from the Residual Channel Attention Block (RCAB) [76] and propose the FRCAB, which is strategically placed at each layer of the decoding stage.

The FRCAB integrates two key components: the residual-in-residual (RIR) structure [76] and Fourier channel attention (FCA), as shown in Fig. 5. The RIR enables the decoder to focus more on high-frequency information, while FCA extracts inter-channel statistics to further enhance the model's capability to discriminate global information.

As illustrated in Fig. 5, given an input feature  $x \in C \times H \times W$ , the FRCAB operates as follows: First, a global vector is extracted using global average pooling  $GAP(\cdot)$  after processing  $x$  with a  $CLC_3(\cdot)$  with  $3 \times 3$  kernel size. Then, a fast Fourier transform in the channel dimension (CFFT) is performed and  $CLC_1(\cdot)$  operations are used to enhance the amplitude  $a^x \in (\frac{C}{2}+1) \times 1 \times 1$  and phase  $p^x \in (\frac{C}{2}+1) \times 1 \times 1$  components of  $x$ . Subsequently, an inverse CFFT (ICFFT) is performed, and two residual connections are constructed. Finally, we employ a  $DNRU(\cdot)$  to reduce the number of channels and up-sampling features, and obtain the output  $y$ . The FRCAB can be mathematically described as:

$$x^c = CFFT(GAP(CLC_3(x))), \quad (22)$$

$$a^x = Amp(x^c), p^x = Pha(x^c), \quad (23)$$

$$a^{xc} = a^x \times GAP(CLC_1(x)), \quad (24)$$

$$p^{xc} = p^x \times GAP(CLC_1(x)), \quad (25)$$

$$x^{ic} = ICFFT(Complex(a^{xc}, p^{xc})) \times CLC_3(x) + x, \quad (26)$$

$$y = DNRU(x^{ic}). \quad (27)$$

where  $\times$  is element-wise multiplication.

After applying the FRCAB in the decoding stage, guided by the clear edge features  $e_3$  generated by the FEB (Sec. III-C),

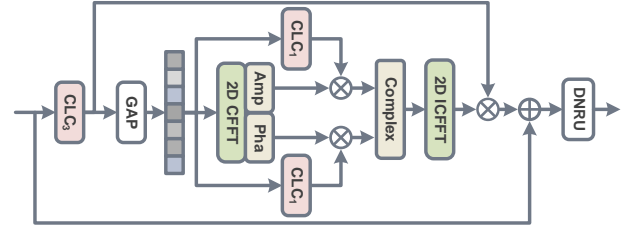


Fig. 5. Architecture of the Fourier Residual Channel Attention Block (FRCAB).

the decoding process proceeds as follows to generate the final saliency map  $\mathcal{S}$ :

$$d_4 = FRCAB(f_4), \quad (28)$$

$$d_3 = FRCAB(Concat(f_3, d_4)), \quad (29)$$

$$d_2 = FRCAB(Concat(f_2, d_3, UP_2(d_4))), \quad (30)$$

$$d_1 = FRCAB(Concat(f_1, d_2, UP_2(d_3), UP_4(d_4))), \quad (31)$$

$$\mathcal{S} = DNRU(Concat(d_1, e_3)), \quad (32)$$

where  $\{d_i\}_{i=1}^4$  and  $\{f_i\}_{i=1}^4$  stand for decoder features and fusion features obtained by the MPA (Sec. III-B).

#### E. Bi-domain Learning

We trained our DFENet with various learning strategies in the spatial and frequency domains, aiming to generate accurate saliency maps and reliable edge features.

1) *Frequency Domain Learning*: As the model deepens, important visual details can be lost, and spectral bias may hinder the model's ability to learn high-accuracy edge features. To address these problems, we propose Co-focus Frequency Loss (CFL), designed to provide effective guidance for FEB (Sec. III-C). CFL leverages fast Fourier transform (FFT) to measure distances in Fourier domain while cross-referencing details in the original feature space. This allows for the optimization of global information and aids FEB in addressing difficult frequencies.

For every pixel  $(u, v)$  in the frequency domain, CFL is defined as:

$$\mathcal{L}_{CFL} = \frac{1}{HW} \sum_{u=0}^{H-1} \sum_{v=0}^{W-1} w |FFT(\mathcal{E}) - FFT(E)|^2, \quad (33)$$

where

$$\mathcal{E} = UP_2(DConv_3(e_3)), \quad (34)$$

and  $E$  denotes the edge of objects in ground-truth  $G$ , obtained by the Canny operator [77].

To focus learning on hard frequencies, we introduce the Co-focus Frequency Matrix (CFM)  $w$  to enhance their associated weights. As discussed in Sec. III-C, the phase component contains plentiful edge frequencies. Thus, while adopting  $r_1$  and  $t_1$  as co-directors, we set amplitude components of  $r_1$ ,  $t_1$  to the mean values to emphasize their phase components. CFM is expressed as:

$$\mathcal{R} = UP_4(DConv_3(r_1)), \mathcal{T} = UP_4(DConv_3(t_1)), \quad (35)$$

$$\tilde{\mathcal{R}} = \text{Complex}(\text{mean}(\text{Amp}(\text{FFT}(\mathcal{R}))), \text{Pha}(\text{FFT}(\mathcal{R}))) \quad (36)$$

$$\tilde{\mathcal{T}} = \text{Complex}(\text{mean}(\text{Amp}(\text{FFT}(\mathcal{T}))), \text{Pha}(\text{FFT}(\mathcal{T}))) \quad (37)$$

$$w = \left( \left| \tilde{\mathcal{R}} - \text{FFT}(E) \right| + \left| \tilde{\mathcal{T}} - \text{FFT}(E) \right| + \left| \text{FFT}(\mathcal{E}) - \text{FFT}(E) \right| \right)^\alpha, \quad (38)$$

where  $\alpha$  is a scaling factor. The introduction of  $r_1$  and  $t_1$  not only provides raw frequency information but also enhances the representation of edge information in the original feature space of both modalities.

2) *Spatial Domain Learning*: We employ  $\mathcal{L}_{BCE}$  to supervise the learning of  $\mathcal{E}$  in the spatial domain:

$$\mathcal{L}_E = \mathcal{L}_{BCE}(\mathcal{E}, E). \quad (39)$$

In addition, to alleviate network bias and ensure the accuracy of the features in the decoding stage, we construct a multi-level loss with  $\mathcal{L}_{BCE}$  and  $\mathcal{L}_{IoU}$ :

$$\mathcal{L}_D = \sum_{i=1}^4 \left( \mathcal{L}_{BCE}(\text{UP}(\text{DCConv}_3(d_i)), G) + \mathcal{L}_{IoU}(\text{UP}(\text{DCConv}_3(d_i)), G) \right) \quad (40)$$

Similarly, the saliency loss is defined as:

$$\mathcal{L}_S = \mathcal{L}_{BCE}(S, G) + \mathcal{L}_{IoU}(S, G). \quad (41)$$

In summary, the total loss  $\mathcal{L}_{total}$  for training is denoted as:

$$\mathcal{L}_{total} = \lambda_1 \mathcal{L}_S + \lambda_2 \mathcal{L}_D + \lambda_3 \mathcal{L}_E + \lambda_4 \mathcal{L}_{CFL}, \quad (42)$$

where  $\{\lambda_i\}_{i=1}^4$  denote weight parameters corresponding to different losses. In this paper, we set them to 1.

## IV. EXPERIMENTS

### A. Experimental Setup

1) *Datasets*: To demonstrate the effectiveness of our proposed DFENet, we conducted a series of experiments on four RGB-T SOD benchmark datasets, namely VT821 [11], VT1000 [12], VT5000 [13], and VI-RGBT1500 [14]. The VT821 dataset consists of 821 pairs of RGB-T images captured under different environmental conditions. The VT1000 dataset comprises 1000 aligned RGB-T images with detailed annotations tailored for evaluation, providing a reliable benchmark for performance comparison. The VT5000 dataset offers 5000 pairs of high-resolution, low-bias RGB-T images that cover a broad range of challenging scenes. The VI-RGBT1500 dataset consists of 1500 RGB-T image pairs captured under different illuminations to validate the benefits of incorporating thermal modality. Following previous works [22], [61], we used 2500 RGB-T image pairs from the VT5000 dataset as our training set, while the remaining images and those from the other three datasets served as our testing set.

2) *Evaluation Metrics*: To comprehensively evaluate the results of each experiment, we employed six widely used evaluation metrics. The E-measure [78] ( $Em$ ) considers both image-level statistics and local pixel differences between the predictions and the ground-truths. The S-measure [79] ( $Sm$ ) evaluates the structural similarity between the predictions and

TABLE I  
SELECTION OF SCALING FACTOR  $\alpha$  IN CO-FOCUS FREQUENCY LOSS. THE BEST RESULTS ARE LABELED **RED**.

Settings	VT821		VT1000		VT5000		VI-RGBT1500	
	$F_\beta \uparrow$	$\mathcal{M} \downarrow$						
$\alpha = 0.5$	0.866	0.025	0.901	0.016	0.871	0.025	0.886	0.028
$\alpha = 1.0$	<b>0.872</b>	<b>0.024</b>	<b>0.905</b>	<b>0.015</b>	<b>0.881</b>	<b>0.024</b>	0.891	0.027
$\alpha = 1.5$	0.863	0.025	0.903	<b>0.015</b>	0.876	0.025	<b>0.893</b>	<b>0.026</b>
$\alpha = 2.0$	0.859	0.026	0.892	0.016	0.869	0.026	0.878	0.031

the ground-truths. The F-measure [80] ( $F_\beta$ ) is a comprehensive metric, calculated by weighted harmonic averaging on precision and recall. We also used the weighted F-measure [81] ( $wF_\beta$ ) to complement the F-measure, addressing issues such as interpolation defects and dependency defects. Additionally, we calculated the Mean absolute error [82] ( $\mathcal{M}$ ), which represents the average discrepancy between each pixel in the prediction and the ground-truth. Finally, Precision-recall (PR) curve [22] is drawn based on precision-recall pairs, where curves closer to (1, 1) indicate better model performance.

3) *Implementation Details*: The backbone of DFENet was initialized with the training parameters of CDFFormer-m [66], while the remaining parameters were initialized using Kaiming initialization [83]. The model was trained on an NVIDIA Tesla P100 GPU with 16GB of memory using Adam optimization [84] and a batch size of 3. Training lasted for 200 epochs, starting with an initial learning rate of  $3 \times 10^{-5}$ , which decayed to one-tenth every 100 epochs. We set the input size to  $384 \times 384$ , and performed a series of data augmentation operations like random cropping, horizontal flipping, and multi-angle rotation to prevent overfitting.

The hyperparameters of CFL, specifically the scaling factor  $\alpha$  in Eq. (38), were determined through careful testing. We fixed  $\alpha = 1$  for our experiments, unless stated otherwise. The representative values of  $\alpha$  used in the tests are presented in Table I.

### B. Model Comparison

To validate the effectiveness of the proposed DFENet, we conducted a comprehensive comparison with fifteen state-of-the-art (SOTA) RGB-T SOD models, namely CSRNet [62], MIDD [56], OSRNet [63], SwinNet [19], ADF [13], TNet [61], MGAI [14], LSNet [33], IFFNet [18], HRTNet [20], CAVER [22], WaveNet [26], LAFB [58], CAFNet [59], and VST++ [25]. To ensure a fair comparison, all saliency maps used for the model comparison were acquired from the corresponding papers' homepages or by running open-source code.

1) *Quantitative Evaluation*: Table II and Fig. 6 presented the quantitative comparison of our DFENet with fifteen existing models using six evaluation metrics:  $Em$ ,  $Sm$ ,  $wF_\beta$ ,  $F_\beta$ ,  $\mathcal{M}$ , and PR curve. In summary, DFENet outperformed existing models across all six metrics on all four benchmark datasets. Specifically, our DFENet surpassed the previously top-performing WaveNet across all four datasets, achieving average improvements of 0.6%, 0.3%, 0.9%, 1.1%, 2.2% in  $Em$ ,  $Sm$ ,  $wF_\beta$ ,  $F_\beta$ , and  $\mathcal{M}$ , respectively. On the more

TABLE II  
 COMPARISON OF E-MEASURE ( $Em$ ), S-MEASURE ( $Sm$ ), F-MEASURE ( $F_\beta$ ), WEIGHTED F-MEASURE ( $wF_\beta$ ), AND MEAN ABSOLUTE ERROR ( $\mathcal{M}$ ) BETWEEN OUR DFENET AND STATE-OF-THE-ART RGB-T SOD MODELS ON VT821, VT1000, VT5000, AND VI-RGBT1500 DATASETS. THE BEST RESULTS ARE LABELED **RED** AND THE SECOND BEST RESULTS ARE LABELED **BLUE**.

Model	Backbone	VT821					VT1000					VT5000					VI-RGBT1500					Param(M)	FLOPs(G)
		$Em \uparrow$	$Sm \uparrow$	$wF_\beta \uparrow$	$F_\beta \uparrow$	$\mathcal{M} \downarrow$	$Em \uparrow$	$Sm \uparrow$	$wF_\beta \uparrow$	$F_\beta \uparrow$	$\mathcal{M} \downarrow$	$Em \uparrow$	$Sm \uparrow$	$wF_\beta \uparrow$	$F_\beta \uparrow$	$\mathcal{M} \downarrow$	$Em \uparrow$	$Sm \uparrow$	$wF_\beta \uparrow$	$F_\beta \uparrow$	$\mathcal{M} \downarrow$		
CSRNet <sub>21</sub> [62]	ESPNetv2	0.908	0.885	0.821	0.830	0.038	0.925	0.918	0.878	0.877	0.024	0.905	0.868	0.797	0.811	0.042	-	-	-	-	-	4.6	4.2
MIDD <sub>21</sub> [56]	VGG-16	0.895	0.871	0.760	0.804	0.045	0.933	0.915	0.856	0.822	0.027	0.897	0.868	0.763	0.801	0.043	0.870	0.762	0.665	0.765	0.069	52.4	257.9
OSRNet <sub>22</sub> [63]	VGG-16	0.896	0.875	0.801	0.813	0.043	0.935	0.926	0.891	0.892	0.022	0.908	0.875	0.807	0.823	0.040	0.917	0.872	0.811	0.836	0.044	42.4	15.6
SwinNet <sub>22</sub> [19]	Swin-B	0.926	0.904	0.818	0.847	0.030	0.947	0.938	0.894	0.896	0.018	0.942	0.912	0.846	0.865	0.026	0.948	0.901	0.863	0.882	0.031	198.7	124.3
ADF <sub>23</sub> [13]	VGG-16	0.842	0.810	0.626	0.716	0.077	0.921	0.910	0.804	0.847	0.034	0.891	0.864	0.722	0.778	0.048	-	-	-	-	-	83.1	77.6
TNet <sub>23</sub> [61]	ResNet-50	0.919	0.899	0.841	0.842	0.030	0.937	0.929	0.895	0.889	0.021	0.927	0.895	0.840	0.846	0.033	0.943	0.894	0.855	0.869	0.034	87.0	39.7
MGA1 <sub>23</sub> [14]	ResNet-50	0.913	0.891	0.824	0.829	0.031	0.935	0.929	0.893	0.885	0.021	0.915	0.883	0.815	0.824	0.034	0.938	0.881	0.834	0.862	0.038	86.8	94.2
LSNet <sub>23</sub> [33]	MobileNetv2	0.911	0.878	0.809	0.825	0.033	0.935	0.925	0.887	0.885	0.023	0.915	0.877	0.806	0.825	0.037	0.935	0.883	0.835	0.859	0.037	5.4	1.2
IFFNet <sub>23</sub> [18]	Segformer	0.918	0.907	0.849	0.848	0.029	0.947	0.938	0.912	0.900	0.017	0.938	0.905	0.856	0.864	0.028	-	-	-	-	-	-	-
HRTNet <sub>23</sub> [20]	HRFormer	0.929	0.906	0.849	0.853	0.026	0.945	0.938	0.913	0.900	0.017	0.945	0.912	0.870	0.871	0.025	0.947	0.899	0.870	0.892	0.030	58.9	17.3
CAVER <sub>23</sub> [22]	ResNet-101	0.929	0.898	0.846	0.854	0.026	0.949	0.938	0.912	0.906	0.016	0.935	0.900	0.849	0.856	0.028	0.949	0.900	0.868	0.881	0.029	93.8	63.9
WaveNet <sub>23</sub> [26]	WaveMLP	0.929	0.912	0.863	0.857	0.024	0.952	0.945	0.921	0.909	0.015	0.940	0.912	0.865	0.867	0.026	0.951	0.909	0.874	0.879	0.027	80.7	64.0
LAFB <sub>24</sub> [58]	Res2Net-50	0.915	0.884	0.817	0.842	0.034	0.945	0.932	0.905	0.905	0.018	0.931	0.893	0.841	0.857	0.030	-	-	-	-	-	453.0	139.7
CAFCNet <sub>24</sub> [59]	ResNet-50	0.927	0.891	0.845	0.856	0.028	0.951	0.935	0.915	0.913	0.017	0.939	0.900	0.858	0.869	0.027	-	-	-	-	-	-	-
VST++ <sub>24</sub> [25]	Swin-B	0.921	0.904	0.850	0.848	0.030	0.951	0.943	0.920	0.908	0.016	0.945	0.915	0.873	0.875	0.025	-	-	-	-	-	217.7	-
DFENet (Ours)	CDFFormer-m	0.938	0.916	0.873	0.872	0.024	0.956	0.945	0.924	0.905	0.015	0.947	0.916	0.876	0.881	0.024	0.955	0.912	0.882	0.891	0.027	149.6	139.5

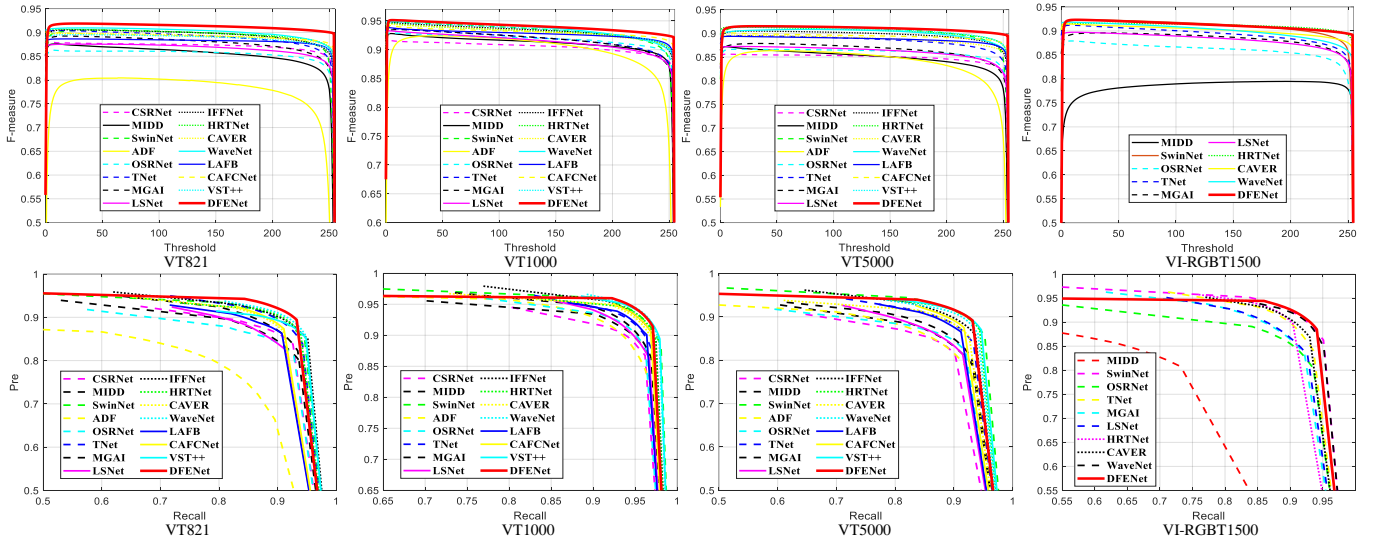


Fig. 6. F-measure curves and precision-recall (PR) curves of the proposed DFENet and fifteen existing models on the VT821, VT1000, VT5000, and VI-RGBT1500 datasets.

challenging VT821, VT5000, and VI-RGBT1500 datasets, the improvements in  $wF_\beta$ ,  $F_\beta$ , and  $\mathcal{M}$  were even more significant, with gains of 1.1%, 1.6%, and 2.6%, respectively. This advantage could be attributed to the rational design of our DFENet, which enables superior global information discrimination. Meanwhile, the proposed Co-focus Frequency Loss (CFL) provides support in optimizing global frequencies and resolving hard frequency problems.

In addition, the comparison of F-measure and PR curves in Fig. 6 further validated the leading performance of our DFENet. In the 1<sup>st</sup> row, F-measure curves of DFENet demonstrated the highest  $F_\beta$  across various thresholds. In the 2<sup>nd</sup> row, PR curves of DFENet were closer to the point with coordinates (1,1) compared to those of other models. These findings indicate DFENet’s superior balance between precision and recall.

2) *Qualitative Evaluation*: Fig. 7 illustrated the saliency maps generated by our proposed DFENet and the fifteen exist-

ing models. It is evident that our DFENet can more accurately detect salient objects in various complex scenes. Even in cases where one modality fails locally (2<sup>nd</sup>-3<sup>rd</sup>, 6<sup>th</sup>-7<sup>th</sup> rows) or both modalities provide poor-quality information (2<sup>nd</sup> and 7<sup>th</sup>-8<sup>th</sup> rows), DFENet can mitigate noise and extraneous contextual cues, enabling precise delineation of salient objects from the background. This is because our proposed MPA reliably captures long-range dependencies and effectively utilizes bi-modal complementary information. Moreover, in fine-grained object detection, existing models, including WaveNet, often incur losses in object depiction. In contrast, DFENet excels in capturing intricate object details, such as the legs of a dog (5<sup>th</sup> row), a person on a motorcycle (7<sup>th</sup> row), and the frame of a chair (10<sup>th</sup> row). This superior performance can be attributed to the collaboration of our proposed DFENet’s components, namely FEB, FRCAB, and CFL. FEB provides reliable edge details through the depth frequency decomposition of low-level features. FRCAB enhances the model’s robustness, improving

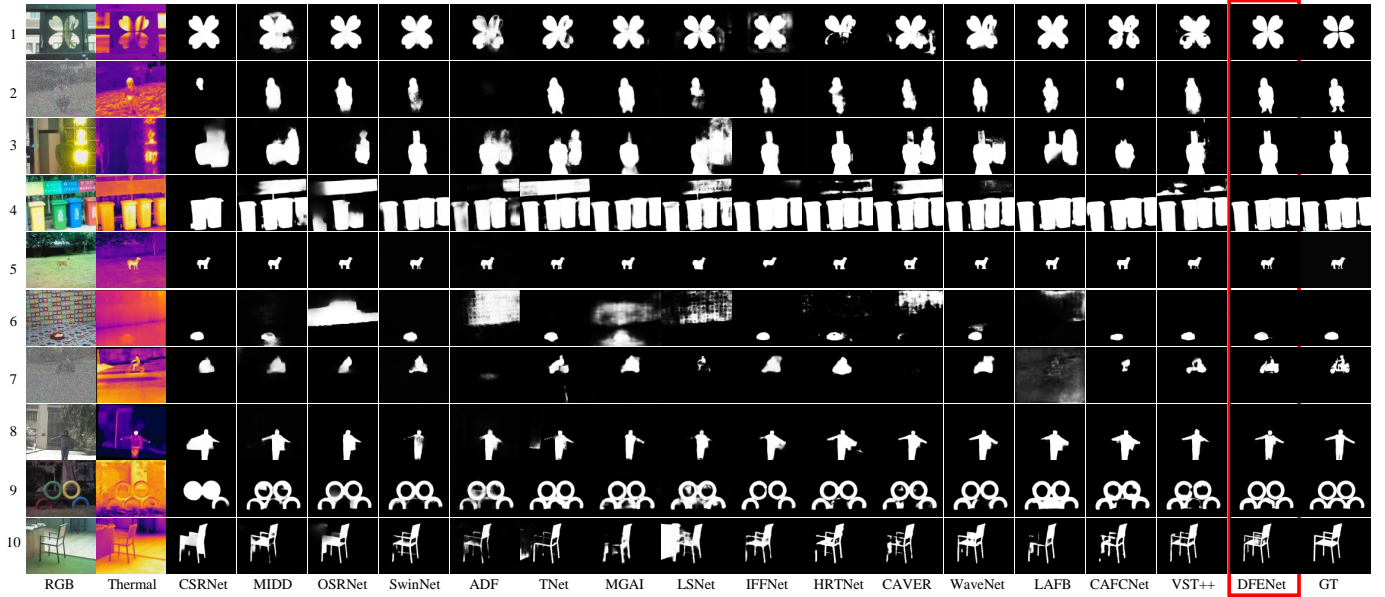


Fig. 7. Visual comparison of our DFENet with fifteen existing models in various complex scenarios, including large objects ( $1^{st}$ - $3^{rd}$ ,  $10^{th}$  rows), small objects ( $5^{th}$ - $7^{th}$  rows), multiple objects ( $4^{th}$  and  $9^{th}$  rows), complex background ( $1^{st}$ - $4^{th}$ ,  $6^{th}$  and  $8^{th}$  rows), low light or contrast ( $3^{rd}$  and  $8^{th}$  rows), small thermal difference ( $2^{nd}$ - $3^{rd}$ ,  $6^{th}$ - $7^{th}$ , and  $9^{th}$  rows), low-quality RGB images ( $2^{nd}$  and  $7^{th}$  rows), and fine-grained objects ( $5^{th}$ ,  $7^{th}$ , and  $10^{th}$  rows). GT stands for ground-truth.

TABLE III

ABLATION STUDY OF EACH COMPONENT IN OUR DFENET. THE BEST RESULTS ARE LABELED RED AND THE SECOND BEST ARE LABELED BLUE.

Type	Settings	VT821				VT1000				VT5000				VI-RGBT1500				Params(M)	FLOPs(G)				
		$E_m \uparrow$	$S_m \uparrow$	$wF_\beta \uparrow$	$F_\beta \uparrow$	$\mathcal{M} \downarrow$	$E_m \uparrow$	$S_m \uparrow$	$wF_\beta \uparrow$	$F_\beta \uparrow$	$\mathcal{M} \downarrow$	$E_m \uparrow$	$S_m \uparrow$	$wF_\beta \uparrow$	$F_\beta \uparrow$	$\mathcal{M} \downarrow$	$E_m \uparrow$			$S_m \uparrow$	$wF_\beta \uparrow$	$F_\beta \uparrow$	$\mathcal{M} \downarrow$
Backbone	w/ GFNet-H-B	0.896	0.865	0.746	0.771	0.046	0.915	0.883	0.852	0.858	0.036	0.887	0.836	0.745	0.784	0.045	0.876	0.796	0.706	0.774	0.062	136.5	129.1
	w/ AFNO	0.913	0.877	0.778	0.806	0.039	0.932	0.912	0.876	0.877	0.026	0.915	0.871	0.798	0.822	0.038	0.916	0.853	0.782	0.820	0.048	132.7	138.0
	w/ DFFormer-m	0.926	0.909	0.858	0.857	0.026	<b>0.958</b>	<b>0.945</b>	<b>0.923</b>	0.903	<b>0.015</b>	<b>0.947</b>	<b>0.917</b>	<b>0.875</b>	<b>0.881</b>	<b>0.024</b>	<b>0.955</b>	<b>0.914</b>	<b>0.884</b>	<b>0.893</b>	<b>0.026</b>	151.3	138.0
Module	w/o MPA	0.925	0.908	0.855	0.855	0.026	0.952	0.941	0.918	0.896	<b>0.016</b>	0.942	0.910	0.863	0.874	0.026	0.949	0.906	0.872	0.878	0.028	144.2	137.9
	w/ MHCA	0.912	0.898	0.836	0.843	0.029	0.946	0.940	0.909	0.886	0.018	0.936	0.903	0.851	0.862	0.029	0.929	0.885	0.834	0.851	0.038	146.3	138.8
	w/o FRCAB	0.927	0.904	0.846	0.849	0.028	0.954	0.943	0.916	0.896	<b>0.016</b>	0.941	0.906	0.855	0.867	0.028	0.951	0.908	0.868	0.883	0.030	127.1	77.4
	w/ RCAB	0.929	0.908	0.857	0.865	0.027	0.954	<b>0.945</b>	<b>0.923</b>	0.904	<b>0.015</b>	<b>0.946</b>	0.914	0.874	0.878	<b>0.025</b>	0.952	0.909	0.880	0.886	<b>0.027</b>	148.1	139.5
	w/o FEB	0.927	<b>0.911</b>	0.854	0.849	0.027	0.954	<b>0.946</b>	0.916	0.889	<b>0.016</b>	0.945	<b>0.916</b>	0.864	0.868	0.026	0.950	<b>0.912</b>	0.870	0.879	0.029	148.6	135.6
w/o CFL	<b>0.932</b>	0.909	<b>0.863</b>	0.865	<b>0.024</b>	0.955	0.943	0.922	<b>0.911</b>	<b>0.015</b>	<b>0.946</b>	0.913	0.873	0.879	<b>0.024</b>	0.952	0.907	0.878	0.888	0.028	149.6	139.5	
Input size	$384^2 \rightarrow 512^2$	0.930	0.909	0.862	<b>0.867</b>	0.026	0.951	0.942	0.919	<b>0.912</b>	<b>0.015</b>	0.945	0.913	0.873	<b>0.884</b>	<b>0.025</b>	<b>0.954</b>	0.910	0.881	<b>0.893</b>	<b>0.026</b>	149.6	248.0
	Full model	<b>0.938</b>	<b>0.916</b>	<b>0.873</b>	<b>0.872</b>	<b>0.024</b>	<b>0.956</b>	<b>0.945</b>	<b>0.924</b>	0.905	<b>0.015</b>	<b>0.947</b>	<b>0.916</b>	<b>0.876</b>	<b>0.881</b>	<b>0.024</b>	<b>0.955</b>	<b>0.912</b>	<b>0.882</b>	<b>0.891</b>	<b>0.027</b>	149.6	139.5

its performance in various scenes. More critically, CFL effectively addresses the problem of lost visual signals and hard frequencies unattended in the frequency domain.

### C. Ablation Study

To comprehensively assess the effectiveness of each component in our proposed DFENet, we conducted ablation studies by comparing models with (w/) and without (w/o) these components, and replacing them with classical methods that operate similarly. The quantitative and qualitative evaluations of ablation studies are shown in Table III, Fig. 8, and Fig. 9.

1) *Effectiveness of backbone network*: To validate the effectiveness of CDFFormer-m [66] as the backbone of DFENet, we compared it with three other FFT-based backbones, namely GFNet-H-B [64], AFNO [65], and DFFormer-m [66]. Notably, AFNO has the same dimension and depth as CDFFormer-m. As shown in the  $1^{st}$ - $2^{nd}$  rows of Table III, the model with GFNet-H-B and AFNO yielded unsatisfactory results, with inferior performance across all four datasets compared to

the model with CDFFormer-m. This trend was further highlighted in Fig. 8, where these models struggled to accurately detect salient objects. Meanwhile, the model with DFFormer-m demonstrated uneven performance on the four datasets. Although it exhibited a slight advantage on the VI-RGBT1500 dataset ( $3^{rd}$  row of Table III), it substantially lagged behind the model with CDFFormer-m on the VT821 dataset.

In addition, we attempted to apply spatial domain-based backbones to DFENet, such as VGG [85], ResNet [86], and Swin Transformer [17]. However, instability (loss reported as “Nan”) occurred during training due to gradient instability caused by the incompatibility of the spatial domain operations and the two Fourier transform operations in MPA.

2) *Effectiveness of MPA (Sec. III-B)*: First, we removed MPA and employed element-wise addition to fuse the bi-modal features, labeled “w/o MPA” in Table III and Fig. 8. The performance of the model lacking MPA declined obviously on the four datasets due to its inability to extract complementary information. In Fig. 8, when the salient region in one or both modalities showed a different appearance, the model

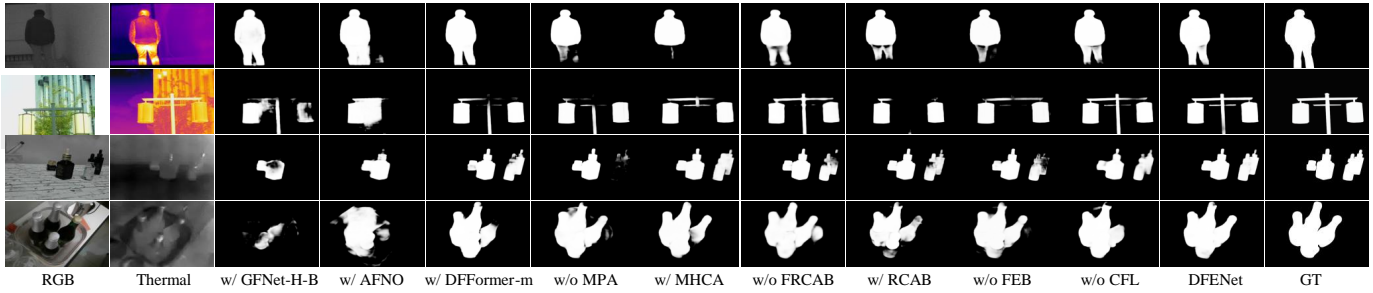


Fig. 8. Visualization results of ablation experiments. GT is ground-truth.

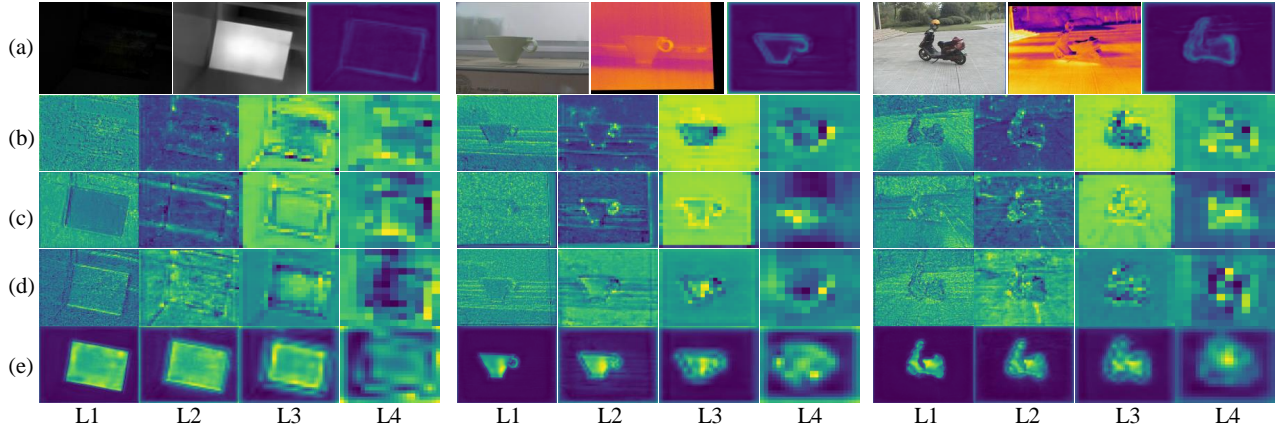


Fig. 9. Visualization of the feature maps pre- and post-processed by each component. L1 to L4 indicates the layers from low to high. (a) shows RGB images, thermal images, and the feature map after FEB. (b) and (c) stand for RGB and thermal feature maps generated by the encoder. (d) represents the fused feature map obtained by MPA. (e) is the feature maps after FRCAB.

without MPA encountered considerable interference, impeding accurate detection of complete objects.

To further validate the effectiveness of the Modal-coordinated Perception Filter (MPF), the core of MPA, we replaced MPF with the widely used multi-head cross-attention (MHCA) [7], [22]. Due to the considerable complexity and memory demands of MHCA, we applied it only to the last three low-resolution layers, while the largest resolution layer still employed element-wise addition. As shown in the 5<sup>th</sup> row of Table III and Fig. 8, the model with MHCA did not perform as well as expected, and even had less gain than the model with element-wise addition. The experiments highlight the suboptimal performance of MHCA compared to MPA in high-resolution feature fusion and demonstrate the incompatibility of spatial-domain operations with frequency-domain models.

Finally, we visualized in Fig. 9 the feature changes after processing by MPA. Even in instances of localized failure within the RGB (e.g., case 1) or thermal modalities (e.g., cases 2 and 3), MPA demonstrated remarkable resilience, successfully fusing both modalities without succumbing to noise interference. The outcomes of the above experiments collectively reinforce the high efficacy of MPA.

3) *Effectiveness of FRCAB (Sec. III-D)*: To verify the effectiveness of the proposed FRCAB, we first replaced it with  $DNRU(\cdot)$  in Eq. (21), labeled “w/o FRCAB” in Table III and Fig. 8. The results showed a significant decrease in metrics  $Em$ ,  $Sm$ ,  $wF_\beta$ ,  $F_\beta$ , and  $\mathcal{M}$ , with an average reduction

of 0.6%, 0.8%, 2.0%, 1.5%, and 13.3%, respectively. The visualization results confirmed this conclusion, revealing that the model would be more susceptible to cluttered backgrounds, lighting variations, and thermal imbalances without FRCAB.

Subsequently, we replaced FRCAB with Residual Channel Attention Block (RCAB) [76], labeled “w/ RCAB” in Table III and Fig. 8. Comparing the 7<sup>th</sup> and last rows of Table III, we found that while the RCAB-equipped model performs well, it consistently falls short of the FRCAB-equipped model across all metrics. This clearly demonstrates that FRCAB can stably improve the model’s robustness and performance compared to RCAB in our DFENet.

As shown in Fig. 9, the features fused by MPA are further refined and decoded by FRCAB. By acquiring channel-wise dependencies, FRCAB enables the model to prioritize high-frequency information and gradually generate high-resolution features.

4) *Effectiveness of FEB (Sec. III-C)*: To validate the gains made by the proposed FEB, we replaced its core component Edge Frequency Extraction Block (EFEB) with  $DNR(\cdot)$  in Eq. (21), while retaining the FRCAB in it, and presented the results in the 8<sup>th</sup> row of Table III. The comparison revealed that without EFEB, all metrics of the model exhibit a decrease to varying degrees. Furthermore, the visualization results depicted in Fig. 8 failed to portray complete object boundaries. In contrast, as illustrated in Fig. 9(a), the complete FEB can consistently provide accurate edge features, regardless of the

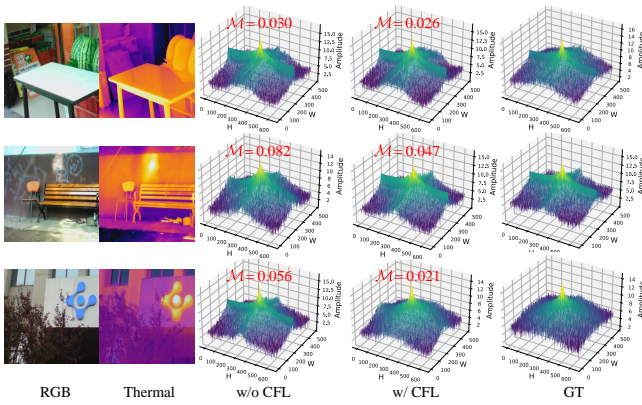


Fig. 10. Frequency spectrum visualization of results from the model training with (w/) and without (w/o) CFL. GT stands for ground-truth.

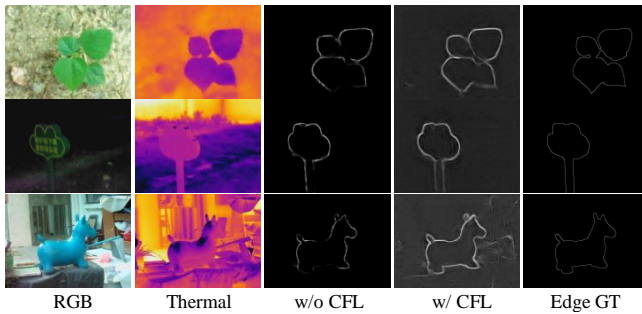


Fig. 11. Visual comparison of edge maps between the model (w/) and without (w/o) CFL. Edge GT stands for the ground-truth of edge.

complexity of the scene. This ability to capture precise edge information offers a powerful boost to the model.

5) *Effectiveness of CFL (Sec. III-E)*: To evaluate the contribution of CFL, we removed it and kept only BCE to supervise the learning of the edge map, denoted as “w/o CFL” in Table III, Fig. 8 and 11. The results showed a degradation in performance on the three datasets after losing the supervision of CFL.

Moreover, we displayed the 3D frequency spectrum of the results obtained with both settings in Fig. 10. It can be seen that 3D spectrograms constructed without CFL supervision exhibit oscillations and frequency distributions that deviate further from the ground-truth. Conversely, the presence of CFL optimizes the loss of frequency reconstruction and brings the frequency statistics closer to ground-truth.

Furthermore, we presented a visual comparison of the edge maps for the two settings in Fig. 11. Even when both modalities provide clear objects (*i.e.*, cases in the 1<sup>st</sup> and 2<sup>nd</sup> rows), the model trained only with BCE still focuses more on edge locations with high priority, making it difficult to detect complete object edges. In contrast, the model supervised with additional CFL not only demonstrates trustworthy performance in typical scenarios but also presents explicit object edges by learning difficult frequencies and reducing frequency gaps, even when object edges are difficult to distinguish from cluttered backgrounds. In conclusion, these findings strongly demonstrate the effectiveness of CFL in learning accurate edge maps and its importance in DFENet.

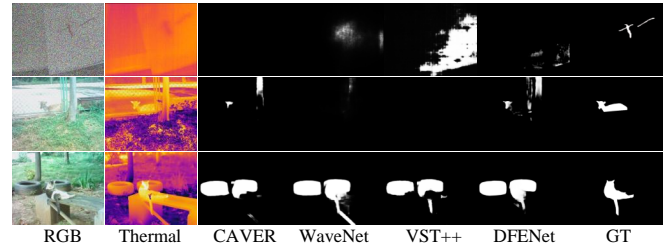


Fig. 12. Failure cases of the proposed DFENet. GT denotes ground-truth.

6) *Increase input resolution*: To verify the effectiveness of DFENet in handling high-resolution bi-modal images, we increased the input resolution to 512<sup>2</sup>. A comparison of the last two rows in Table III showed that the 512<sup>2</sup> resolution model has comparable performance to the 384<sup>2</sup> resolution model on the VT1000, VT5000, and VI-RGBT1500 datasets, and a slight degradation on the VT821 dataset. This performance degradation is mainly caused by the small input resolution of the pre-trained encoder used in our practice. Notably, this is the first attempt at high-resolution RGB-T SOD, whereas existing RGB-T SOD models typically have input resolution ranging from 224<sup>2</sup> to 384<sup>2</sup>.

#### D. Complexity Analysis

We presented the number of parameters (Params) and the floating point operations (FLOPs) of RGB-T SOD models and each component of DFENet in Table II and Table III. Overall, the proposed DFENet is a heavyweight model. Compared to knowledge-distillation-based WaveNet [26], DFENet has better performance, but has 68.9M more Params and 75.5G more FLOPs, making it only slightly smaller than WaveNet’s teacher network, SwinNet [19]. While compared to the purely Transformer-based VST++ [25], we have a 31.3% reduction in Params. Specifically, most of DFENet’s computational cost comes from the backbone network, while our two proposed components, namely MPA and FEB contribute minimally. The MPA increases only 5.4M Params and 1.6G FLOPs compared to element-wise addition, whereas the FEB just requires 1.0M Params and 3.9G FLOPs. Additionally, the complexity of FRCAB is nearly identical to RCAB, with a 1.5M increase in Params overall.

#### E. Limitations and Future Works

Despite achieving outstanding performance, our DFENet still struggles with some complex scenarios. As shown in Fig. 12, DFENet erroneously identifies salient objects when the background exhibits more discriminative features than foreground objects, such as higher regional contrast, greater temperature change, and faster gradient change. In contrast, due to the existence of the category concept, it is easier for the human attention mechanism to focus on central objects or living organisms while ignoring cluttered backgrounds. To mimic this mechanism, future improvements could involve adding prompts such as text and audio, or introducing large models to get more discriminating information.

Furthermore, while FFT-based operations demonstrate remarkable potential, their integration with spatial-domain operations remains an open challenge due to compatibility issues. Integrating spatial-domain techniques alongside FFT could enhance the model's ability to capture local features and handle irregular object shapes. Therefore, combining FFT- and spatial domain-based techniques holds promising research prospects and merits further attention.

## V. CONCLUSION

In this paper, we proposed DFENet to explore the potential of fast Fourier Transform (FFT) in solving RGB and thermal salient object detection (RGB-T SOD). Specifically, to fully bridge the complementary information and fuse the RGB and thermal modalities, we designed the Modal-coordinated Perception Attention (MPA), which embeds channel FFT into spatial Fourier components, achieving deep-level and multi-dimensional representation enhancement. Compared to conventional multi-head self-attention-based operations, MPA can be easily applied to high-resolution bi-modal feature fusion. In the decoding stage, we proposed the Frequency-decomposed Edge-aware Block (FEB) and Fourier Residual Channel Attention Block (FRCAB) to achieve high-resolution salient maps. Based on the analysis of bi-modal frequency decomposition, we presented FEB to clarify accurate object edges from the background and guide the integration of decoder features. We then deployed FRCAB in each decoder layer to focus on high-frequency information and obtain global dependencies in the channel dimension of the frequency domain. In the training stage, we proposed the Co-focus Frequency Loss (CFL) to assist FEB in solving hard frequencies and enhance edge representations within the bi-modal feature spaces. This frequency-domain learning synergized with spatial-domain learning to realize high-quality salient maps. Extensive experiments demonstrated that DFENet surpassed fifteen existing RGB-T SOD models on four benchmark datasets and exhaustively exhibited the representation capabilities of FFT-based operations, providing a new paradigm for a series of SOD tasks.

## REFERENCES

- [1] C. Guo and L. Zhang, "A novel multiresolution spatiotemporal saliency detection model and its applications in image and video compression," *IEEE Trans. Image Process.*, vol. 19, no. 1, pp. 185–198, 2010.
- [2] C. F. Flores, A. Gonzalez-Garcia, J. van de Weijer, and B. Raducanu, "Saliency for fine-grained object recognition in domains with scarce training data," *Pattern Recogn.*, vol. 94, pp. 62–73, 2019.
- [3] Y. Shi, S. Zhao, J. Wu, Z. Wu, and H. Yan, "Fixated object detection based on saliency prior in traffic scenes," *IEEE Trans. Circuits Syst. Video Technol.*, vol. 34, no. 3, pp. 1413–1426, 2024.
- [4] H. Zhou, B. Qiao, L. Yang, J. Lai, and X. Xie, "Texture-guided saliency distilling for unsupervised salient object detection," in *Proc. CVPR*, 2023, pp. 7257–7267.
- [5] Y. Wang, R. Wang, X. Fan, T. Wang, and X. He, "Pixels, regions, and objects: Multiple enhancement for salient object detection," in *Proc. CVPR*, 2023, pp. 10031–10040.
- [6] H. Wang, L. Wan, and H. Tang, "Leno: Adversarial robust salient object detection networks with learnable noise," in *Proc. AAAI*, vol. 37, no. 2, 2023, pp. 2537–2545.
- [7] N. Liu, N. Zhang, K. Wan, L. Shao, and J. Han, "Visual saliency transformer," in *Proc. ICCV*, 2021, pp. 4722–4732.
- [8] W. Ji, J. Li, S. Yu, M. Zhang, Y. Piao, S. Yao, Q. Bi, K. Ma, Y. Zheng, H. Lu *et al.*, "Calibrated rgb-d salient object detection," in *Proc. CVPR*, 2021, pp. 9471–9481.
- [9] W. Ji, J. Li, Q. Bi, Chuan guo, J. Liu, and L. Cheng, "Promoting saliency from depth: Deep unsupervised RGB-d saliency detection," in *Proc. ICLR*, 2022.
- [10] J. Wu, F. Hao, W. Liang, and J. Xu, "Transformer fusion and pixel-level contrastive learning for rgb-d salient object detection," *IEEE Trans. Multimedia*, 2023.
- [11] G. Wang, C. Li, Y. Ma, A. Zheng, J. Tang, and B. Luo, "Rgb-t saliency detection benchmark: Dataset, baselines, analysis and a novel approach," in *Proc. IGTA*, 2018, pp. 359–369.
- [12] Z. Tu, T. Xia, C. Li, X. Wang, Y. Ma, and J. Tang, "Rgb-t image saliency detection via collaborative graph learning," *IEEE Trans. Multimedia*, vol. 22, no. 1, pp. 160–173, 2020.
- [13] Z. Tu, Y. Ma, Z. Li, C. Li, J. Xu, and Y. Liu, "Rgbt salient object detection: A large-scale dataset and benchmark," *IEEE Trans. Multimedia*, vol. 25, pp. 4163–4176, 2023.
- [14] K. Song, L. Huang, A. Gong, and Y. Yan, "Multiple graph affinity interactive network and a variable illumination dataset for rgbt image salient object detection," *IEEE Trans. Circuits Syst. Video Technol.*, vol. 33, no. 7, pp. 3104–3118, 2023.
- [15] A. Vaswani, N. Shazeer, N. Parmar, J. Uszkoreit, L. Jones, A. N. Gomez, L. Kaiser, and I. Polosukhin, "Attention is all you need," in *Proc. NIPS*, vol. 30, 2017.
- [16] A. Dosovitskiy, L. Beyer, A. Kolesnikov, D. Weissenborn, X. Zhai, T. Unterthiner, M. Dehghani, M. Minderer, G. Heigold, S. Gelly, J. Uszkoreit, and N. Houlsby, "An image is worth 16x16 words: Transformers for image recognition at scale," in *Proc. ICLR*, 2021.
- [17] Z. Liu, Y. Lin, Y. Cao, H. Hu, Y. Wei, Z. Zhang, S. Lin, and B. Guo, "Swin transformer: Hierarchical vision transformer using shifted windows," in *Proc. ICCV*, 2021, pp. 10012–10022.
- [18] K. Song, Y. Bao, H. Wang, L. Huang, and Y. Yan, "A potential vision-based measurements technology: Information flow fusion detection method using rgb-thermal infrared images," *IEEE Trans. Instrum. and Meas.*, vol. 72, pp. 1–13, 2023.
- [19] Z. Liu, Y. Tan, Q. He, and Y. Xiao, "Swinnet: Swin transformer drives edge-aware rgb-d and rgb-t salient object detection," *IEEE Trans. Circuits Syst. Video Technol.*, vol. 32, no. 7, pp. 4486–4497, 2022.
- [20] B. Tang, Z. Liu, Y. Tan, and Q. He, "Hrtransnet: Hrformer-driven two-modality salient object detection," *IEEE Trans. Circuits Syst. Video Technol.*, vol. 33, no. 2, pp. 728–742, 2023.
- [21] G. Chen, F. Shao, X. Chai, H. Chen, Q. Jiang, X. Meng, and Y.-S. Ho, "Cgmdnet: Cross-guided modality difference reduction network for rgb-t salient object detection," *IEEE Trans. Circuits Syst. Video Technol.*, vol. 32, no. 9, pp. 6308–6323, 2022.
- [22] Y. Pang, X. Zhao, L. Zhang, and H. Lu, "Caver: Cross-modal view-mixed transformer for bi-modal salient object detection," *IEEE Trans. Image Process.*, vol. 32, pp. 892–904, 2023.
- [23] H. Zhou, C. Tian, Z. Zhang, C. Li, Y. Ding, Y. Xie, and Z. Li, "Position-aware relation learning for rgb-thermal salient object detection," *IEEE Trans. Image Process.*, 2023.
- [24] F. Sun, P. Ren, B. Yin, F. Wang, and H. Li, "Catnet: A cascaded and aggregated transformer network for rgb-d salient object detection," *IEEE Trans. Multimedia*, 2023.
- [25] N. Liu, Z. Luo, N. Zhang, and J. Han, "Vst++: Efficient and stronger visual saliency transformer," *IEEE Transactions on Pattern Analysis and Machine Intelligence*, 2024.
- [26] W. Zhou, F. Sun, Q. Jiang, R. Cong, and J.-N. Hwang, "Wavenet: Wavelet network with knowledge distillation for rgb-t salient object detection," *IEEE Trans. Image Process.*, vol. 32, pp. 3027–3039, 2023.
- [27] M. Frigo and S. G. Johnson, "Fftw: An adaptive software architecture for the fft," in *Proc. ICASSP*, vol. 3, 1998, pp. 1381–1384.
- [28] J. Huang, Y. Liu, F. Zhao, K. Yan, J. Zhang, Y. Huang, M. Zhou, and Z. Xiong, "Deep fourier-based exposure correction network with spatial-frequency interaction," in *Proc. ECCV*, 2022, pp. 163–180.
- [29] C. Li, C.-L. Guo, man zhou, Z. Liang, S. Zhou, R. Feng, and C. C. Loy, "Embedding fourier for ultra-high-definition low-light image enhancement," in *Proc. ICLR*, 2023.
- [30] C. Wang, H. Wu, and Z. Jin, "Fourllie: Boosting low-light image enhancement by fourier frequency information," in *Proc. ACM MM*, 2023, pp. 7459–7469.
- [31] J. Huang, M. Zhou, D. Li, B. Li, C.-L. Guo, and C. Li, "Revitalizing channel-dimension fourier transform for image enhancement," 2024.
- [32] N. Rahaman, A. Baratin, D. Arpit, F. Draxler, M. Lin, F. Hamprecht, Y. Bengio, and A. Courville, "On the spectral bias of neural networks," in *Proc. ICML*, 2019, pp. 5301–5310.

- [33] W. Zhou, Y. Zhu, J. Lei, R. Yang, and L. Yu, "Lsnet: Lightweight spatial boosting network for detecting salient objects in rgb-thermal images," *IEEE Trans. Image Process.*, vol. 32, pp. 1329–1340, 2023.
- [34] T.-Y. Lin, P. Goyal, R. Girshick, K. He, and P. Dollár, "Focal loss for dense object detection," in *Proc. ICCV*, 2017, pp. 2980–2988.
- [35] L. Jiang, B. Dai, W. Wu, and C. C. Loy, "Focal frequency loss for image reconstruction and synthesis," in *Proc. ICCV*, 2021, pp. 13919–13929.
- [36] X. Hu, Y. Cai, J. Lin, H. Wang, X. Yuan, Y. Zhang, R. Timofte, and L. Van Gool, "Hdnet: High-resolution dual-domain learning for spectral compressive imaging," in *Proc. CVPR*, 2022, pp. 17542–17551.
- [37] S. Woo, J. Park, J.-Y. Lee, and I. S. Kweon, "Cbam: Convolutional block attention module," in *Proc. ECCV*, 2018, pp. 3–19.
- [38] Y. Piao, W. Ji, J. Li, M. Zhang, and H. Lu, "Depth-induced multi-scale recurrent attention network for saliency detection," in *Proc. ICCV*, 2019, pp. 7254–7263.
- [39] G. Li, Z. Liu, M. Chen, Z. Bai, W. Lin, and H. Ling, "Hierarchical alternate interaction network for rgb-d salient object detection," *IEEE Trans. Image Process.*, vol. 30, pp. 3528–3542, 2021.
- [40] T. Hussain, A. Anwar, S. Anwar, L. Petersson, and S. W. Baik, "Pyramidal attention for saliency detection," in *Proc. CVPRW*, IEEE, 2022, pp. 2877–2887.
- [41] M. Song, W. Song, G. Yang, and C. Chen, "Improving rgb-d salient object detection via modality-aware decoder," *IEEE Trans. Image Process.*, vol. 31, pp. 6124–6138, 2022.
- [42] Z. Wu, G. Allibert, F. Meriaudeau, C. Ma, and C. Démonceaux, "Hidnet: Rgb-d salient object detection via hierarchical depth awareness," *IEEE Trans. Image Process.*, vol. 32, pp. 2160–2173, 2023.
- [43] Y. Luo, F. Shao, Z. Xie, H. Wang, H. Chen, B. Mu, and Q. Jiang, "Hfmdnet: Hierarchical fusion and multi-level decoder network for rgb-d salient object detection," *IEEE Transactions on Instrumentation and Measurement*, 2024.
- [44] L.-C. Chen, G. Papandreou, I. Kokkinos, K. Murphy, and A. L. Yuille, "DeepLab: Semantic image segmentation with deep convolutional nets, atrous convolution, and fully connected crfs," *IEEE Trans. Pattern Anal. Mach. Intell.*, vol. 40, no. 4, pp. 834–848, 2017.
- [45] Y. Pang, L. Zhang, X. Zhao, and H. Lu, "Hierarchical dynamic filtering network for rgb-d salient object detection," in *Proc. ECCV*, 2020, pp. 235–252.
- [46] X. Cheng, X. Zheng, J. Pei, H. Tang, Z. Lyu, and C. Chen, "Depth-induced gap-reducing network for rgb-d salient object detection: An interaction, guidance and refinement approach," *IEEE Trans. Multimedia*, 2022.
- [47] F. Yu, V. Koltun, and T. Funkhouser, "Dilated residual networks," in *Proc. CVPR*, July 2017.
- [48] J. Zhang, D.-P. Fan, Y. Dai, X. Yu, Y. Zhong, N. Barnes, and L. Shao, "Rgb-d saliency detection via cascaded mutual information minimization," in *Proc. ICCV*, 2021, pp. 4338–4347.
- [49] Y.-f. Zhang, J. Zheng, W. Jia, W. Huang, L. Li, N. Liu, F. Li, and X. He, "Deep rgb-d saliency detection without depth," *IEEE Trans. Multimedia*, vol. 24, pp. 755–767, 2021.
- [50] N. Liu, N. Zhang, L. Shao, and J. Han, "Learning selective mutual attention and contrast for rgb-d saliency detection," *IEEE Trans. Pattern Anal. Mach. Intell.*, vol. 44, no. 12, pp. 9026–9042, 2021.
- [51] S. Yao, M. Zhang, Y. Piao, C. Qiu, and H. Lu, "Depth injection framework for rgb-d salient object detection," *IEEE Trans. Image Process.*, 2023.
- [52] Z. Liu, Y. Wang, Z. Tu, Y. Xiao, and B. Tang, "Tritransnet: Rgb-d salient object detection with a triplet transformer embedding network," in *Proc. ACM MM*, 2021, pp. 4481–4490.
- [53] J. Wang, K. Song, Y. Bao, L. Huang, and Y. Yan, "Cgfnnet: Cross-guided fusion network for rgb-t salient object detection," *IEEE Trans. Circuits Syst. Video Technol.*, vol. 32, no. 5, pp. 2949–2961, 2021.
- [54] Q. Zhang, T. Xiao, N. Huang, D. Zhang, and J. Han, "Revisiting feature fusion for rgb-t salient object detection," *IEEE Trans. Circuits Syst. Video Technol.*, vol. 31, no. 5, pp. 1804–1818, 2020.
- [55] W. Gao, G. Liao, S. Ma, G. Li, Y. Liang, and W. Lin, "Unified information fusion network for multi-modal rgb-d and rgb-t salient object detection," *IEEE Trans. Circuits Syst. Video Technol.*, vol. 32, no. 4, pp. 2091–2106, 2021.
- [56] Z. Tu, Z. Li, C. Li, Y. Lang, and J. Tang, "Multi-interactive dual-decoder for rgb-thermal salient object detection," *IEEE Trans. Image Process.*, vol. 30, pp. 5678–5691, 2021.
- [57] G. Chen, F. Shao, X. Chai, H. Chen, Q. Jiang, X. Meng, and Y.-S. Ho, "Modality-induced transfer-fusion network for rgb-d and rgb-t salient object detection," *IEEE Trans. Circuits Syst. Video Technol.*, vol. 33, no. 4, pp. 1787–1801, 2022.
- [58] K. Wang, Z. Tu, C. Li, C. Zhang, and B. Luo, "Learning adaptive fusion bank for multi-modal salient object detection," *IEEE Trans. Circuits Syst. Video Technol.*, 2024.
- [59] D. Jin, F. Shao, Z. Xie, B. Mu, H. Chen, and Q. Jiang, "Cafcnnet: Cross-modality asymmetric feature complement network for rgb-t salient object detection," *Expert Systems with Applications*, vol. 247, p. 123222, 2024.
- [60] Z. Tu, Z. Li, C. Li, and J. Tang, "Weakly alignment-free rgb-t salient object detection with deep correlation network," *IEEE Trans. Image Process.*, vol. 31, pp. 3752–3764, 2022.
- [61] R. Cong, K. Zhang, C. Zhang, F. Zheng, Y. Zhao, Q. Huang, and S. Kwong, "Does thermal really always matter for rgb-t salient object detection?" *IEEE Trans. Multimedia*, vol. 25, pp. 6971–6982, 2023.
- [62] F. Huo, X. Zhu, L. Zhang, Q. Liu, and Y. Shu, "Efficient context-guided stacked refinement network for rgb-t salient object detection," *IEEE Trans. Circuits Syst. Video Technol.*, vol. 32, no. 5, pp. 3111–3124, 2022.
- [63] F. Huo, X. Zhu, Q. Zhang, Z. Liu, and W. Yu, "Real-time one-stream semantic-guided refinement network for rgb-thermal salient object detection," *IEEE Trans. Instrum. and Meas.*, vol. 71, pp. 1–12, 2022.
- [64] Y. Rao, W. Zhao, Z. Zhu, J. Lu, and J. Zhou, "Global filter networks for image classification," in *Proc. NIPS*, vol. 34, 2021, pp. 980–993.
- [65] J. Guibas, M. Mardani, Z. Li, A. Tao, A. Anandkumar, and B. Catanzaro, "Adaptive fourier neural operators: Efficient token mixers for transformers," *arXiv preprint arXiv:2111.13587*, 2021.
- [66] Y. Tatsunami and M. Taki, "Fft-based dynamic token mixer for vision," in *Proc. AAAI*, vol. 38, no. 14, 2024, pp. 15328–15336.
- [67] M. Zhou, J. Huang, C.-L. Guo, and C. Li, "Former: An efficient global modeling paradigm for image restoration," in *Proc. ICML*, 2023, pp. 42589–42601.
- [68] T. Chu, J. Chen, J. Sun, S. Lian, Z. Wang, Z. Zuo, L. Zhao, W. Xing, and D. Lu, "Rethinking fast fourier convolution in image inpainting," in *Proc. ICCV*, 2023, pp. 23195–23205.
- [69] Z. Wu, Y. Jin, and K. M. Yi, "Neural fourier filter bank," in *Proc. CVPR*, 2023, pp. 14153–14163.
- [70] C. Wang, J. Jiang, Z. Zhong, and X. Liu, "Spatial-frequency mutual learning for face super-resolution," in *Proc. CVPR*, 2023, pp. 22356–22366.
- [71] A. Farshad, Y. Yeganeh, P. Gehlbach, and N. Navab, "Y-net: A spatio-spectral dual-encoder network for medical image segmentation," in *Proc. MICCAI*, 2022, pp. 582–592.
- [72] G. Liu, Z. Chen, D. Liu, B. Chang, and Z. Dou, "Ftmf-net: A fourier transform-multiscale feature fusion network for segmentation of small polyp objects," *IEEE Trans. Instrum. and Meas.*, vol. 72, pp. 1–15, 2023.
- [73] P.-T. De Boer, D. P. Kroese, S. Mannor, and R. Y. Rubinfeld, "A tutorial on the cross-entropy method," *Ann. Oper. Res.*, vol. 134, pp. 19–67, 2005.
- [74] G. Mátyus, W. Luo, and R. Urtasun, "Deeproadmapper: Extracting road topology from aerial images," in *Proc. ICCV*, 2017, pp. 3438–3446.
- [75] W. Yu, M. Luo, P. Zhou, C. Si, Y. Zhou, X. Wang, J. Feng, and S. Yan, "Metaformer is actually what you need for vision," in *Proc. CVPR*, 2022, pp. 10819–10829.
- [76] Y. Zhang, K. Li, K. Li, L. Wang, B. Zhong, and Y. Fu, "Image super-resolution using very deep residual channel attention networks," in *Proc. ECCV*, 2018, pp. 286–301.
- [77] J. Canny, "A computational approach to edge detection," *IEEE Trans. Pattern Anal. Mach. Intell.*, no. 6, pp. 679–698, 1986.
- [78] D.-P. Fan, C. Gong, Y. Cao, B. Ren, M.-M. Cheng, and A. Borji, "Enhanced-alignment measure for binary foreground map evaluation," in *Proc. IJCAI*, 7 2018, pp. 698–704.
- [79] D.-P. Fan, M.-M. Cheng, Y. Liu, T. Li, and A. Borji, "Structure-measure: A new way to evaluate foreground maps," in *Proc. ICCV*, 2017, pp. 4558–4567.
- [80] R. Achanta, S. Hemami, F. Estrada, and S. Susstrunk, "Frequency-tuned salient region detection," in *Proc. CVPR*, 2009, pp. 1597–1604.
- [81] R. Margolin, L. Zelnik-Manor, and A. Tal, "How to evaluate foreground maps," in *Proc. CVPR*, 2014, pp. 248–255.
- [82] F. Perazzi, P. Krähenbühl, Y. Pritch, and A. Hornung, "Saliency filters: Contrast based filtering for salient region detection," in *Proc. CVPR*, 2012, pp. 733–740.
- [83] K. He, X. Zhang, S. Ren, and J. Sun, "Delving deep into rectifiers: Surpassing human-level performance on imagenet classification," in *Proc. ICCV*, 2015, pp. 1026–1034.
- [84] D. P. Kingma and J. Ba, "Adam: A method for stochastic optimization," *arXiv preprint arXiv:1412.6980*, 2014.
- [85] K. Simonyan and A. Zisserman, "Very deep convolutional networks for large-scale image recognition," *arXiv preprint arXiv:1409.1556*, 2014.
- [86] K. He, X. Zhang, S. Ren, and J. Sun, "Deep residual learning for image recognition," in *Proc. CVPR*, 2016, pp. 770–778.